JGR Oceans

RESEARCH ARTICLE
10.1029/2022JC018463

Heat Flux Estimates From a Synthesis of Satellite Observations and a Hydrodynamic Model (With Application to Long Island Sound)

Grant McCardell[1], Rachel Horwitz[2], Amin Ilia[1,3], M. Kay Howard Strobel[1], Todd Fake[1], and James O'Donnell[1,4]

[1]Department of Marine Sciences, University of Connecticut, Groton, CT, USA, [2]Fisheries and Oceans, Bedford Institute of Oceanography, Dartmouth, NS, Canada, [3]CoreLogic, Oakland, CA, USA, [4]Connecticut Institute for Resilience and Climate Adaptation, University of Connecticut, Groton, CT, USA

Key Points:

- We infer net air-sea heat fluxes by assimilating satellite measurements of sea surface temperatures into a calibrated hydrodynamic model
- We estimate both surface heat fluxes and horizontal exchange fluxes
- We describe the annual evolution of the heat budget in Long Island Sound, USA

Correspondence to:

G. McCardell,
grant.mccardell@uconn.edu

Citation:

McCardell, G., Horwitz, R., Ilia, A., Howard Strobel, M. K., Fake, T., & O'Donnell, J. (2023). Heat flux estimates from a synthesis of satellite observations and a hydrodynamic model (with application to Long Island Sound). *Journal of Geophysical Research: Oceans*, *128*, e2022JC018463. https://doi.org/10.1029/2022JC018463

Received 13 MAY 2022
Accepted 30 JAN 2023

Abstract Estimating surface heat fluxes via direct covariance measurements or bulk formulae is observation-intensive and costly. We present a methodology whereby we estimate net surface heat fluxes as the difference between the depth-integrated heat tendencies and the depth-integrated horizontal heat exchanges in a hydrodynamic model. We calibrate the model to achieve a good representation of mixing and advection and then assimilate satellite sea surface temperature (SST) observations into the model at an 8-day scale. The SST data assimilation forces a good representation of observed temperatures and heat tendencies both at the surface and throughout the water column. We estimate the horizontal heat exchange directly from the model output and then infer the surface fluxes required to close the budget. When we apply this methodology to a model with prescribed surface heat fluxes and without data assimilation, we can recover the prescribed fluxes with an RMS error of ± 10 W m^{-2} and an r^2 of 0.998. When we compare our results to those estimated using Coupled Ocean-Atmosphere Response Experiment bulk formulae with observations in western Long Island Sound, we find similarly good agreement.

Plain Language Summary We use satellite observations of sea surface temperatures in combination with a three-dimensional simulation of the ocean to infer the air-sea surface heat fluxes needed to create the observed surface temperatures. We use this methodology to quantify the annual cycle of warming and cooling fluxes in Long Island Sound (LIS). Our surface heat flux estimates compare well with estimates obtained from meteorological measurements in the western LIS.

1. Introduction

Estimates of surface heat fluxes in the world's oceans and coastal regions are of paramount importance to our understanding of both inter-annual and intra-annual variability. Seasonal cycles driven by annual variation in surface heat fluxes are ubiquitous in biological, physical, and chemical processes. Obtaining accurate values for surface heat fluxes, particularly for long-term means, is, however, difficult. Starting in 1992, the Coupled Ocean-Atmosphere Response Experiment (COARE) has developed algorithms to estimate ocean surface fluxes from standard meteorological measurements (Fairall et al., 2003). Although estimating surface fluxes using COARE bulk formulae is easier than via the direct covariance measurements they are designed to surrogate, significant meteorological data is nevertheless required.

2. Model Implementation

2.1. Model Background

Other numerical hydrodynamic models of the Long Island Sound (LIS) region include the coastal transport model described by Wilson et al. (2005), the New York Harbor Observing and Prediction System (NYHOPS) model described by Georgas et al. (2016), and the LIS ROMS implementation described by Jia and Whitney (2019). The domain of the Long Island Sound FVCOM model (LIS-FVCOM) described herein is shown in Figure 1. LIS-FVCOM implements the FVCOM model described by Chen et al. (2007) and uses the results of the operational northwest Atlantic regional model, operated as the Northeast Coastal Forecast System (NECOFS), to provide ocean boundary conditions and meteorological forcing. This "nesting" approach is computationally

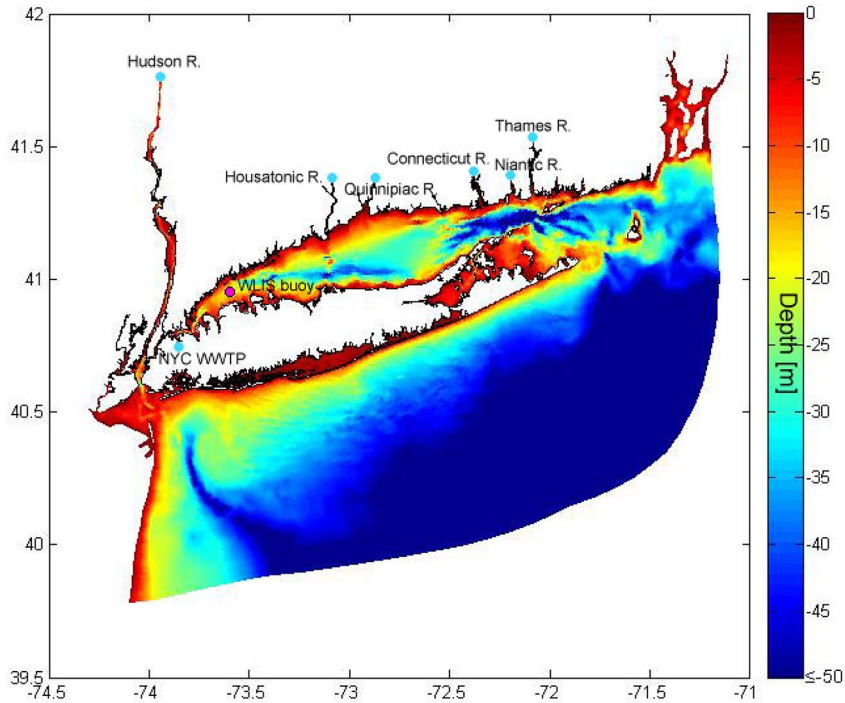

Figure 1. Map of southern New England showing the LIS-FVCOM model grid (colored region). Model bathymetry is shown by the color scale and the locations of freshwater sources are shown by light blue dots (from left to right: Hudson River, New York City wastewater treatment plants, Housatonic River, Quinnipiac River, Connecticut River, Niantic River, and Thames River). The location of the western Long Island Sound buoy is shown in magenta.

efficient since it allows the effect of the larger-scale processes to be simulated at coarse resolution through NECOFS and allows LIS-FVCOM computing resources to focus on the smaller-scale structures in LIS and Block Island Sound. Figure 1 also shows the bathymetry of the region and the locations of the freshwater sources used in the model. Our implementation uses GOTM (Burchard et al., 1999) to model vertical turbulent mixing. O'Donnell et al. (2015b) found that a bottom roughness value of $z_0 = 1$ cm provided the best representation of bed stresses within LIS in the FVCOM model and this value was used throughout the entire domain.

2.2. Initial Conditions

LIS-FVCOM was initialized for 2012 using a temperature and salinity climatology data set derived via objective interpolation (OI) of Connecticut Department of Energy and Environmental Protection (CTDEEP) station data as described by O'Donnell et al. (2015b), and data in the NOAA archive as described by Codiga and Ullman (2011). These fields were then linearly interpolated to the LIS-FVCOM grid. The 2013 model runs were initialized using end-of-year conditions from the 2012 run.

2.3. Sea Surface Height Forcing

LIS-FVCOM is forced at the seaward boundaries by sea level variations and salinity and temperature. The sea level was initially prescribed using tidal constituents derived from the global tidal model (Egbert et al., 1994). Since the Egbert et al. (1994) constituents are not precise in shelf areas, the amplitudes and phase of the major constituents were iteratively adjusted to improve the representation of the amplitude and phase at each tidal frequency using NOAA tidal height observations from 2010 at Montauk (NY), New London (CT), New Haven (CT), Bridgeport (CT), and King's Point (NY). Each constituent amplitude and phase was adjusted by the proportional amplitude error and phase error to improve the model. Subtidal fluctuations at the open boundary are incorporated from the NECOFS system by de-tiding and low-pass filtering the NECOFS solution at the open boundary locations using t-tide (Pawlowicz et al., 2002) and a 25-hr raised cosine low-pass filter. The NECOFS subtidal

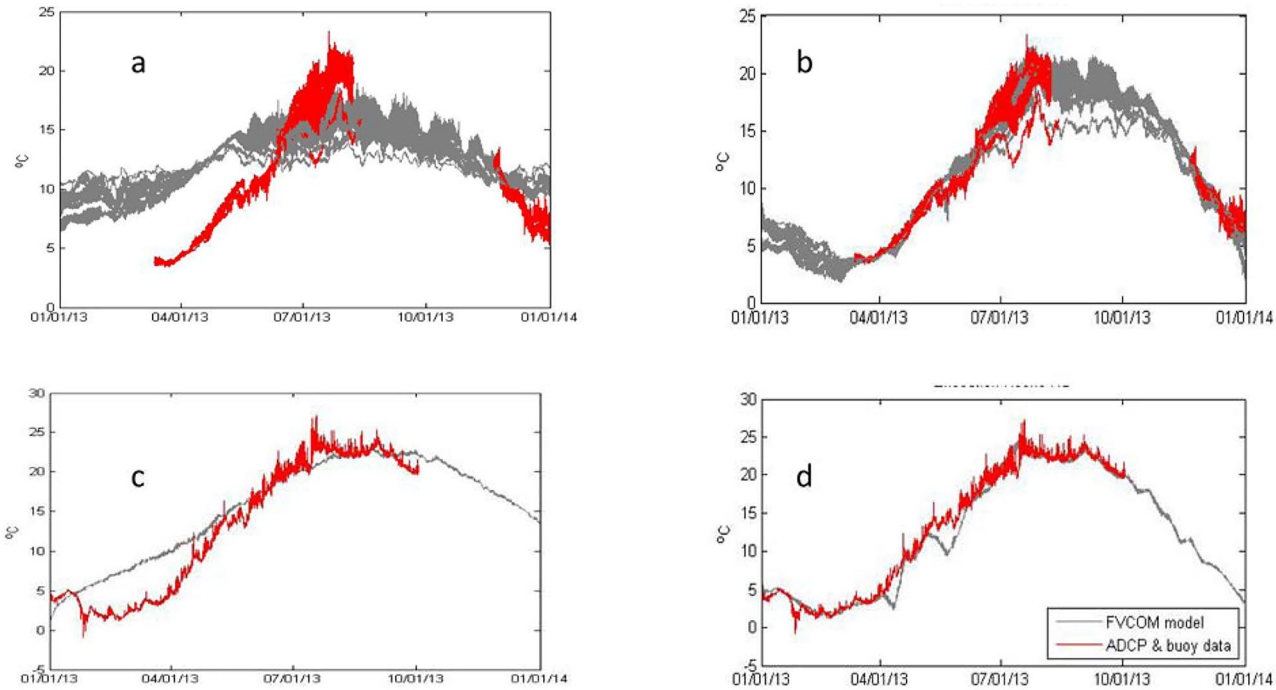

Figure 2. Comparison of model temperature predictions (gray) with observations (red) in Long Island Sound (LIS) during 2013 with and without sea surface temperature (SST) data assimilation. (a, c) show comparisons when the model is forced using only Weather Research and Forecasting heat fluxes; (b, d) show the comparisons when MODIS-a SST is also assimilated into the model. (a, b) show comparisons of near-bottom temperatures at seven locations in the ELIS and Block Island Sound during 2013 (see O'Donnell et al., 2015a); (c, d) show comparisons of near-surface temperatures at the LISICOS Execution Rocks buoy.

solution was then combined with a time series of tidal heights generated using the improved open-boundary tidal constituents.

2.4. Wind Stress Forcing

The LIS-FVCOM model is forced using domain-variable winds derived from the Weather Research and Forecasting (WRF) model run as hindcasts at UMass, Dartmouth as part of the New England Coastal Ocean Forecast System (NECOFS). (See https://comt.ioos.us/projects/necofs_transition for more details).

2.5. Model Freshwater Inputs

Freshwater enters the LIS-FVCOM domain through seven model cells corresponding to the locations of the Thames, Connecticut, Niantic, Quinnipiac, Housatonic, and Hudson rivers and New York City wastewater treatment plants (WWTPs) (see Figure 1 for locations). These fluxes are based on flow rates, R_i, measured by the USGS at Thompsonville, CT, and lagged by 1 day to account for the distance between the head of the Connecticut River in our model and Thompsonville. Each R_i is adjusted using the USGS Thompsonville data as $R_i = 1.20 R_{CT}\left(\overline{R_i}/\overline{R_{CT}}\right)$ where R_{CT} is the day-specific Connecticut River flow, $\overline{R_{CT}}$ is the mean Connecticut River flow, and $\overline{R_i}$ is the mean flow for river i. The factor of 1.20 follows from the salt budget of Gay et al. (2004) and accounts for the portion of the watersheds of the rivers below the USGS gauges. A fixed input of 40 $m^3\ s^{-1}$ was added to the East River to represent the freshwater discharged from New York WWTPs.

2.6. Heat Forcing and SST Data Assimilation

LIS-FVCOM uses heat fluxes obtained from the NECOFS WRF model. However, the NECOFS WRF heat fluxes substantially underestimated the fall and winter cooling at LIS locations as evidenced by unrealistically high wintertime water temperatures (e.g., Figures 2a and 2c). To offset this limitation, we assimilated sea surface temperatures (SSTs) into the model using 4 km NASA MODIS Aqua 8-day composited and de-clouded (level

3) night-time satellite data (OBPG, 2015). SST was assimilated into the surface sigma layer using a nudging approach. This form of SST data assimilation adds small corrections to the LIS-FVCOM surface layer temperatures based on their differences to the SST values. See Chen et al. (2013) for further details. A nudging factor was chosen such that the time scale of the nudging was at or above the 8-day time scale of the SST satellite observations. The NECOFS WRF data set was still used for direct heat forcing of the model. In this way, short-term variations in the surface heat fluxes that are well-represented in WRF such as those due to diel insolation cycles or intermittent cloud cover are preserved while longer-term bias errors such as those due to misestimation of latent fluxes in the WRF model are corrected before they can create unrealistic model temperatures.

Because the NASA SST product has erratic coverage in cells that are close to the coast, we pre-screened the entire data set to keep only data from cells that had at least 86.7% coverage (i.e., we removed all data from those cells with 7 or more missing 8-day SSTs out of the total of 45 8-day records for the 2013 years). The remaining SST data were first linearly interpolated in time to fill any temporal gaps and then spatially interpolated to fill in any missing cells using the nearest neighboring cell with good coverage. An effect of this pre-screening and interpolation methodology is that values in cells at the coast where coverage is poor are replaced with the values from the nearest offshore cell with good coverage. Note that due to coarse spatial and temporal scales of the satellite data and the need to interpolate missing data, the SST assimilation does not capture fine-scale features such as near-shore shoals or the Connecticut River plume front.

Figure 2 shows time series of model-to-data temperature comparisons both with and without the SST assimilation. Note that the improvement in the bottom temperatures (panels a and b) is similar to the improvement in the surface temperatures (panels c and d), indicating that the model is capturing the downward and horizontal heat fluxes adequately.

3. Model Validation

3.1. Skill Metrics

To assess the quantitative model performance, we use the "skill", s, statistic defined as:

$$s = 1 - \frac{\left\langle (f_m - f_d)^2 \right\rangle}{\left\langle (f_d - \langle f_d \rangle)^2 \right\rangle} \tag{1}$$

where f_m and f_d represent the model and data values (e.g., f represents sea level (η) or temperature (T), etc.) and the $\langle\ \rangle$ notation represents the mean of the argument over the simulation interval (i.e., $<f_d>$ is the mean of the data) (von Storch & Zwiers, 1999). No single measure of model performance provides an ideal summary; however, s has the useful property that it is 1 when the model and data are in perfect agreement and becomes negative when the difference in the model and data is larger than the variance in the data record. Note that since the model predicts the average value in a grid cell while in situ data used for validation are obtained at a much higher resolution, even a perfect model would not generally achieve a skill of 1.

In addition to the model skill described by Equation 1, which we will also refer to as the "traditional skill," another useful metric is the Brier Skill. The Brier Skill is a quantification of inter-model skill comparison that is calculated by normalizing the mean square error in a model by the mean square error in a second "reference model" (Ganju et al., 2016; von Storch & Zwiers, 1999). Like the classic skill metric described above, the Brier skill has a value of 1 when the model and data are in perfect agreement. When the model being evaluated outperforms the reference model, the Brier skill is positive. If the reference model is in closer agreement with the data, then the Brier Skill is negative. If the reference model is taken to be the mean of all the observations, $<f_d>$, the Brier skill is equivalent to Equation 1. If, however, the Brier skill is assessed using a reference model consisting of monthly climatology from 1991 to 2015 CTDEEP surveys at multiple individual locations throughout LIS, then a positive skill score indicates the model outperforms the CTDEEP climatology. Note that outperforming a spatial and seasonal climatology is more difficult than outperforming overall observational means and indicates that the model can represent inter-annual variability.

3.2. Sea Surface Height

Table 1 shows s, the model skill (Equation 1), when compared to hourly measurements at the four NOAA tidal gauges in LIS: New London, New Haven, Bridgeport, and King's Point. The first row shows the skills when sea

Table 1
Traditional Model Skills (Equation 1) When Model Elevations Are Compared to Gauges in LIS at New London, New Haven, Bridgeport, and King's Point

	New London	New Haven	Bridgeport	King's Point
η	0.91	0.92	0.93	0.93
η'	0.94	0.93	0.94	0.94
$<\eta>$	0.77	0.75	0.77	0.54

Note. The first row (η), shows the skills when sea surface heights (relative to MSL) are compared, the second row shows the skills at tidal frequencies (η'), the third row shows the skills for the subtidal residuals ($<\eta>$).

surface heights (relative to MSL) are compared, the second and third rows show the skills when the elevations are decomposed using t_tide (Pawlowicz et al., 2002) into tidal and subtidal components. The table indicates that the model skills at tidal frequencies are substantially greater than the subtidal skills.

Figure 3 shows the 2013 subtidal sea levels at the four NOAA tide gauge stations in LIS (shown in red) compared to the model predictions (shown in blue). Note that in addition to capturing the fluctuations due to winds, the model is also capturing the seasonal summertime increase in sea surface heights that occurs as a result of summertime warming and seasonal changes in wind forcing. The model also captures the along-estuary SSH gradient that results from the along-Sound density gradient and the mean wind stress. Figure 4 shows the model mean along-Sound sea level predictions for 2013 referenced to MSL at New London.

3.3. Temperature and Salinity

Figure 5 shows a comparison of surface and bottom model temperatures and the 2013 CTDEEP surveys with monthly climatologies derived from 1993 to 2015 CTDEEP surveys. These data are described by Kaputa and Olsen (2000) and O'Donnell et al. (2014). The skills listed in the panels were calculated by combining individual station scores using the mean square methodology described by Ganju et al. (2016). The near-surface and near-bottom temperature skills of 0.986 and 0.984 shown in Figure 5 are considerably higher than skills from runs that only used the WRF heat flux forcing (did not use the SST assimilation), which were 0.72 and 0.85, respectively. Note that the CTDEEP data set used to evaluate the temperature skills shown in Figure 5 was not assimilated into the model. The high skill scores are indicative not only of the success of the data assimilation itself but also of excellent agreement between the screened remote sensing temperature data and the in situ temperature measurements made by the CTDEEP. The near-surface and near-bottom traditional salinity skills are 0.63 and 0.85, respectively, with Brier skills of −0.40 and −0.01.

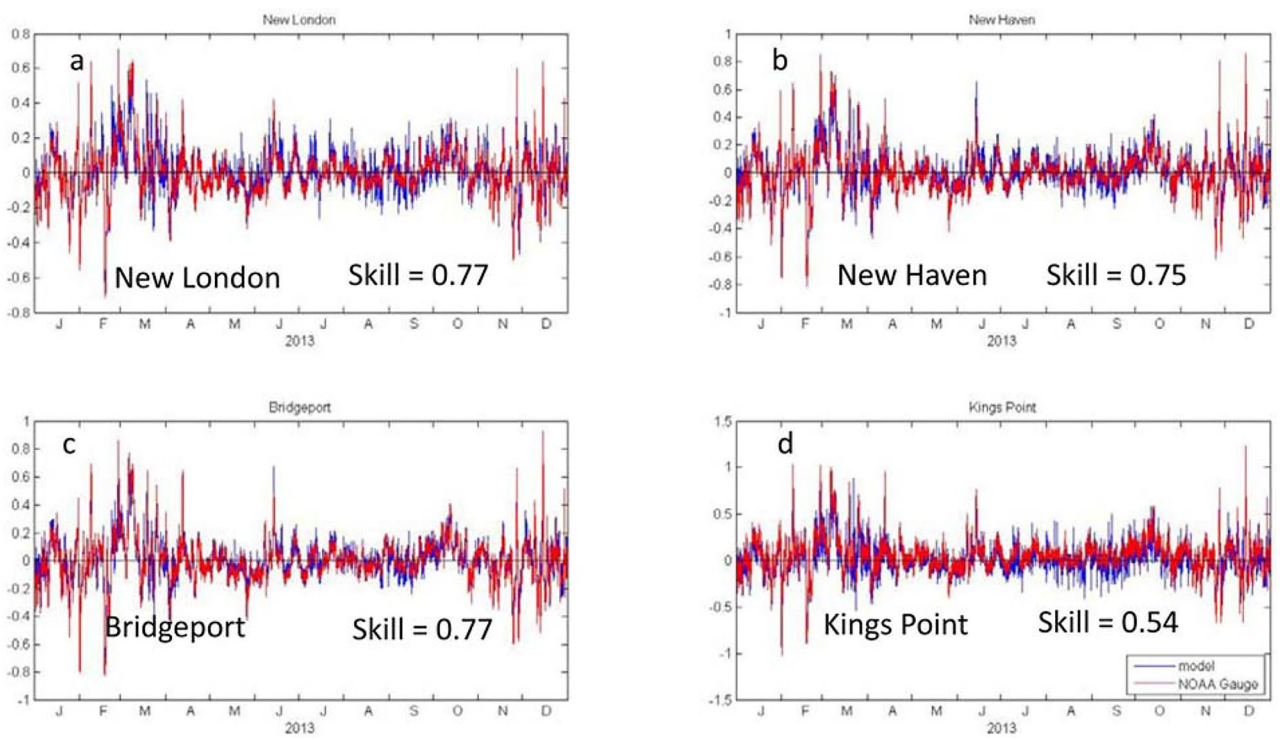

Figure 3. Subtidal sea-level model predictions (blue) compared to NOAA gauge data (red) at the New London (a), New Haven (b), Bridgeport (c), and Kong's Point (d) stations in Long Island Sound.

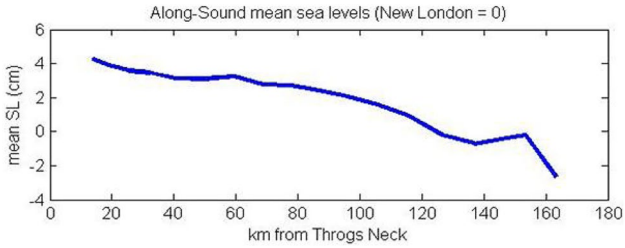

Figure 4. Mean model sea-level predictions (blue) along an along-Sound transect plotted by distance from the head of the Sound at the Throg's Neck.

4. Heat Flux Estimates

4.1. Methodology

Since the model-data temperature agreement is good for both the near-surface and near-bottom layers, it is worthwhile to infer the net surface heat flux fluxes required to produce these temperatures. Assuming no horizontal diffusion (this was set to zero in the model) and ignoring pressure effects, the tendency of the vertically integrated heat content, $H = C_p T \rho$, where $Cp(T,S)$ is the specific heat capacity, T is temperature, and $\rho(T,S)$ is density, will be equal to the downwards surface flux, P, less the downward benthic flux, B, less the vertically integrated advective flux divergence, which can be expressed as

$$\frac{\partial}{\partial t}\int_{-h}^{\eta} H \cdot dz = P - B - \int_{-h}^{\eta} \nabla \cdot (H\mathbf{u}) \cdot dz \tag{2}$$

where h is the water depth, η is the free-surface elevation, and $\boldsymbol{u}$ is the water velocity.

The FVCOM grid consists of a triangular mesh where scalar values are calculated and output at triangle vertices while velocities are calculated and output at the triangle centroids (see Figure 6). Following Chen et al. (2013), we refer to the triangle vertices as "nodes" and the triangles themselves as "cells." The area around each node consisting of the polygon whose points are the centroids of the connected triangles and the midpoints of the connected sides of these triangles is termed the "tracer control element" or TCE. In this scheme, the scalar fluxes

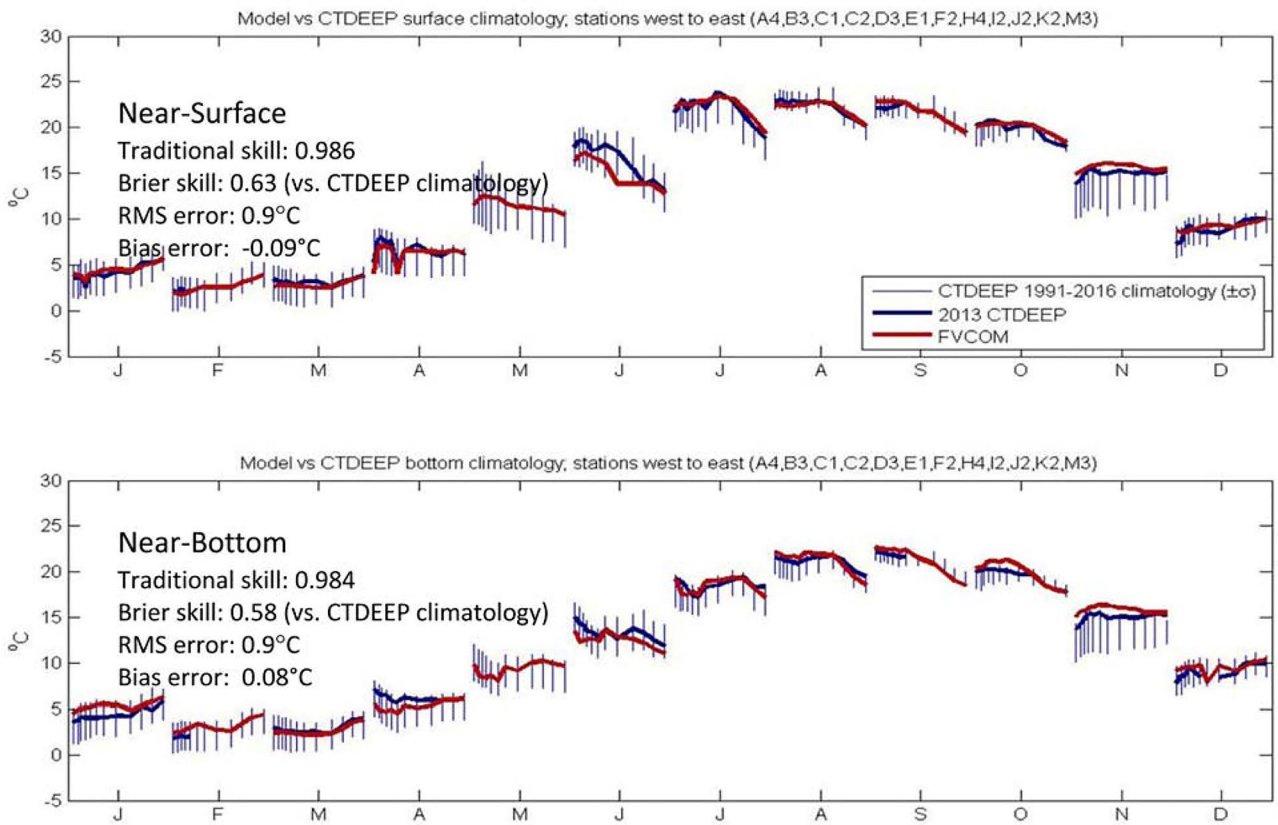

Figure 5. Plots by month showing surface (top panel) and bottom (bottom panel) temperature comparisons between model predictions (red lines) and monthly climatologies from 1993 to 2015 CTDEEP survey data (thin vertical blue bars, ±σ) and the 2013 CTDEEP surveys (thick blue lines). Within each month, the CTDEEP stations are plotted by longitude from west to east.

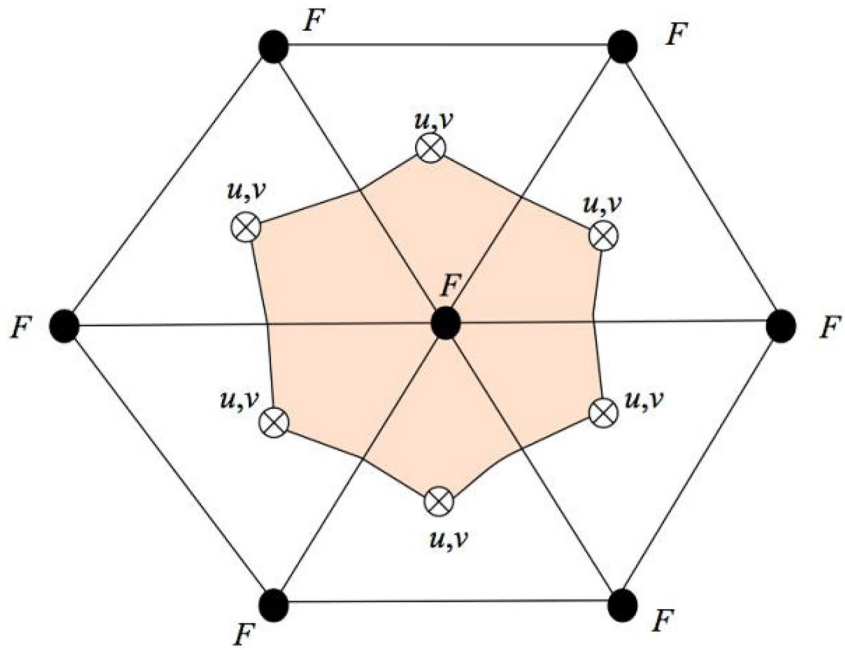

Figure 6. FVCOM unstructured grid. Triangle nodes are shown by solid black circles labeled *F*; centroids are shown by the cross-hatched circles labeled *u*,*v*. The shaded area around the center node is the "tracer control element" or TCE. From Chen et al. (2013).

into or out of the TCE area (shown shaded in Figure 6) are calculated as the sum of the fluxes through the pairs of sections defined by each centroid and the midpoints of the two adjacent sides.

The total volume flux into or out of an individual TCE is then $\sum_{j=1}^{N}\sum_{i=1}^{2} L_{i,j} D_{i,j} \mathbf{u}_{i,j} \cdot \mathbf{n}_{i,j}$ where N is the number of triangles connected to the central TCE node, $L_{i,j}$ are the lengths of the midpoint-to-centroid sections, $D_{i,j}$ are the average layer depths along these sections, and $\mathbf{u}_{i,j} \cdot \mathbf{n}_{i,j}$ are the components of the velocity normal to the sections. According to Green's Theorem, the total volume flux into or out of each TCE must also be equal to the change in the total volume within the TCE. This is easily calculated as $\sigma A \partial\eta/\partial t$ where σ is the normalized layer depth, A is the area of the TCE, and η is the areal-mean free-surface elevation. Equating the total fluxes with the volume change provides:

$$\sum_{j=1}^{N}\sum_{i=1}^{2} L_{i,j} D_{i,j} \mathbf{u}_{i,j} \cdot \mathbf{n}_{i,j} = \sigma \int_{A} \partial\eta/\partial t \cdot dA \tag{3}$$

When we evaluate Equation 3 using model results at hourly intervals, we find small discrepancies between LHS and RHS terms. There are several possible reasons for this small misfit. However, since conservation of mass in FVCOM has been extensively tested (Chen et al., 2007), we also impose volume conservation and rewrite Equation 3 as:

$$\alpha\left(\sum_{j=1}^{N}\sum_{i=1}^{2} L_{i,j} D_{i,j} \mathbf{u}_{i,j} \cdot \mathbf{n}_{i,j}\right) + \beta \approx \sigma \int_{A} \partial\eta/\partial t \cdot dA \tag{4}$$

where $\alpha \approx 1$ and $\beta \approx 0$ are adjustment factors chosen to minimize the misfit between the two sides of Equation 4. While α and β could be obtained using a least-squares approach, estimating these for each cell using the first and second moments of the two sides of Equation 3 is computationally more efficient. For each TCE, we estimate the adjustment factor α by matching the variance of the LHS of Equation 3 to that of the RHS of Equation 3 using the entire year record, that is,

$$\alpha \cong \frac{\sum_{k=1}^{M}\left(\sigma\int_{A}(\partial\eta/\partial t)_k\cdot dA-\frac{1}{M}\sum_{k=1}^{M}\sigma\int_{A}(\partial\eta/\partial t)_k\cdot dA\right)^2}{\sum_{k=1}^{M}\left(\sum_{j=1}^{N}\sum_{i=1}^{2}L_{i,j}D_{i,j,k}\mathbf{u}_{i,j,k}\cdot\mathbf{n}_{i,j}-\frac{1}{M}\sum_{k=1}^{M}\sum_{j=1}^{N}\sum_{i=1}^{2}L_{i,j}D_{i,j,k}\mathbf{u}_{i,j,k}\cdot\mathbf{n}_{i,j}\right)^2} \tag{5}$$

where M is the total number of model-output records in the time dimension. Likewise, the offset (bias) correction, β, is chosen (for each TCE) to match the long-term means of the integrated horizontal volume transports (LHS of Equation 3) with the long-term mean of the volume tendencies (RHS of Equation 3):

$$\beta \cong \frac{1}{M}\sum_{k=1}^{M}\sigma\int_{A}(\partial\eta/\partial t)_k\cdot dA-\frac{1}{\alpha M}\sum_{k=1}^{M}\sum_{j=1}^{N}\sum_{i=1}^{2}L_{i,j}D_{i,j,k}\mathbf{u}_{i,j,k}\cdot\mathbf{n}_{i,j} \tag{6}$$

We use the α and β coefficient approximations obtained from Equations 5 and 6 to estimate the net surface and bottom boundary heat flux, P−B, as the vertical sum over Q layers of the difference between the tendencies and the adjusted horizontal transport:

$$P-B=\sum_{m=1}^{Q}\left(\begin{array}{l}\frac{\alpha}{A}\sum_{j=1}^{N}\sum_{i=1}^{2}H_{j,m}\left(L_{i,j}D_{i,j,m}\mathbf{u}_{i,j,m}\cdot\mathbf{n}_{i,j}+\frac{\beta}{N}\right)\\-\frac{\sigma}{A}\int_{A}(h\partial H/\partial t)_m+(H\partial\eta/\partial t)_m\cdot dA\end{array}\right) \tag{7}$$

Where h is the water depth (i.e., σh is the TCE layer depth). The first term on the RHS of Equation 7 represents the volume-corrected horizontal heat fluxes into or out of the TCE; the second term represents the heat tendency within the TCE. The j subscripts in the first term of Equation 7 indicate that the horizontal transport values are estimated per TCE side and then summed; the tendencies shown by the second term are those within the TCE volume.

4.2. Error Analysis

Model salinity can be used as a conservative tracer in the model to assess methodological errors in using Equation 7. Since there are no surface or bottom salt fluxes in our model, any net salt tendency should be equal to the horizontal flux divergence. Therefore, if Equation 7 is formulated to represent the salt budget, there should be no surface or bottom fluxes and Equation 7 should be identically zero. Any non-zero differences in terms of Equation 7 when evaluated for salt are therefore errors. We normalize the mean square of the error in the integrated salt flux by the variance in the salt tendency and consider the square root of this to be representative of the relative error in the approach and applicable to our surface heat flux estimates:

$$RelSaltErr=\sqrt{\frac{\sum_{m=1}^{Q}\sum_{k=1}^{M}\left(\begin{array}{l}\frac{\sigma}{A}\int_{A}\rho_{k,m}S_{k,m}(\partial\eta/\partial t)_k+h\rho_{k,m}(\partial S/\partial t)_{k,m}\cdot dA\\-\alpha\sum_{j=1}^{N}\sum_{i=1}^{2}\rho_{i,j,k,m}S_{i,j,k,m}\left(L_{i,j,k}D_{i,j,k,m}\mathbf{u}_{i,j,k,m}\cdot\mathbf{n}_{i,j,k}+\frac{\beta}{N_k}\right)\end{array}\right)^2}{\sum_{m=1}^{Q}\sum_{k=1}^{M}\left(\begin{array}{l}\frac{\sigma}{A}\int_{A}\rho_{k,m}S_{k,m}(\partial\eta/\partial t)_k+h\rho_{k,m}(\partial S/\partial t)_{k,m}\cdot dA\\-\frac{1}{M}\sum_{k=1}^{m}\frac{\sigma}{A}\int_{A}\rho_{k,m}S_{k,m}(\partial\eta/\partial t)_k+h\rho_{k,m}(\partial S/\partial t)_{k,m}\cdot dA\end{array}\right)^2}} \tag{8}$$

where S is the salinity. The error bars shown in Figure 8 show estimates of the uncertainties in the heat flux calculations based on Equation 8.

We also assessed whether Equation 7 could reproduce prescribed surface heat fluxes. For model runs that were performed without SST data assimilation, the surface heat fluxes are entirely prescribed by the WRF forcing input file and there are no bottom heat fluxes. Using output from runs without SST assimilation, we examined the differences between these prescribed surface heat fluxes and those obtained using Equation 7. Figure 7 shows a scatter plot comparing the fluxes prescribed by the WRF input files with those inferred using Equation 7. Perfect agreement would indicate that Equation 7 captures all internal FVCOM calculations with 100% accuracy.

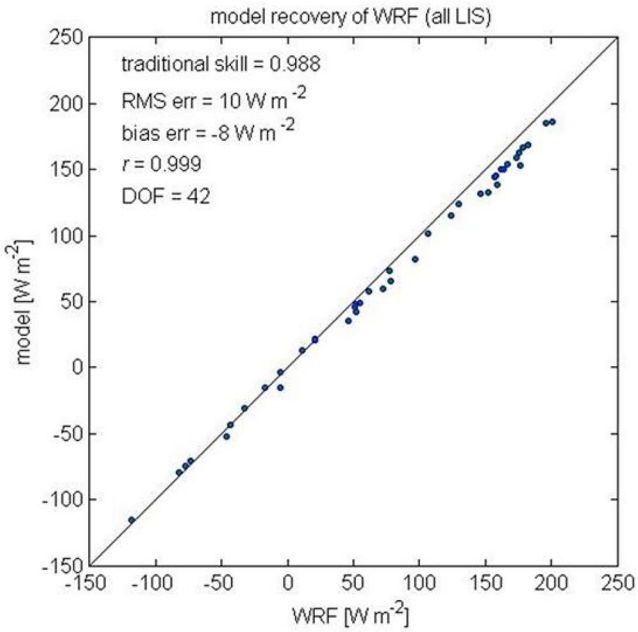

Figure 7. Comparison of prescribed input surface heat fluxes from Weather Research and Forecasting (WRF) (x-axis) with fluxes inferred using the methodology herein (y-axis.).

Although not perfect, the agreement seen in Figure 7 is consistent with the error estimates based on the salt budget and shows an RMS error of only ±10 W m^{-2}. There is a bias of −8 W m^{-2} with a tendency for large fluxes to be slightly underestimated.

4.3. LIS Results

Heat exchanges with the bottom sediment and porewater are expected to be small. We neglect them and equate the surface heat flux to the RHS of Equation 7. Because the grid scale of the LIS-FVCOM model is considerably finer than the resolution of the SST data, the derived fluxes were spatially filtered using an 8 km area-weighted Gaussian filter with weights $w_i = \frac{w_i'}{W}$ where $w_i' = \left(a_i e^{-{d_i}^2/2r^2}|_{d_i<4r};\ 0|_{d_i\geq 4r}\right)$ and $W = \sum_{j=1}^{j=N} w_j'$, r = 8 km, and a_i and d_i are the areas of and distances to the surrounding TCE cells.

Figure 8 shows the monthly mean surface heat fluxes at the LISICOS Western Sound Buoy location (see Figure 1) derived from the LIS-FVCOM model using SST assimilation compared with surface heat flux bulk estimates obtained using buoy measurements of water temperature, air temperature, long and short wave irradiance, relative humidity, and wind speed. The estimation of the surface heat fluxes from observations at this buoy used the COARE bulk formulae of Fairall et al. (2003) and is described in Ilia et al. (2023).

Also shown in Figure 8 is our estimate of the horizontal heat exchange in the model, shown as the depth-integrated horizontal flux divergence, $\int_{-h}^{\eta} \nabla_{x,y} \cdot (H\mathbf{u}_{x,y}) \cdot dz = \int_{-h}^{\eta} \frac{\partial}{\partial x}(Hu) + \frac{\partial}{\partial y}(Hv) \cdot dz$ where $\mathbf{u}_{x,y} = [u, v]$ are the horizontal components of the water velocity. Note that this is the heat change in the water column per unit areal surface and can thereby be compared directly to the surface flux contribution to the depth-integrated heat budget. This estimation of horizontal heat exchange in LIS is a result that cannot be obtained from an analysis of meteorological data on its own and one which neither Lee and Lwiza (2005) nor Ilia et al. (2023) were able to obtain.

5. Discussion

In the summer, LIS warms more than the adjacent shelf waters and, therefore, horizontal heat export from LIS is expected. Likewise, LIS cools more than the adjacent shelf during the winter and will import heat during the winter. Based on an analysis of water-column temperature tendencies in conjunction with surface heat fluxes estimated via bulk formulae, Lee and Lwiza (2005) suggest that inter-annual variability in horizontal heat exchange may be a more important driver of inter-annual temperature anomalies in LIS than the inter-annual variability in the surface heat fluxes. Lee and Lwiza (2005) were, however, unable to quantify horizontal heat exchanges in LIS. Our results (Figure 8) indicate that during the period of summertime warming in May–July 2013, 50–100 W m^{-2} of heat was exported from the WLIS buoy location (see Figure 1) on average. As noted previously, this is expressed per square meter of water surface so as to be directly comparable with the surface flux. This summertime export is substantial and represents about a third of the surface flux. Figure 8 also indicates that from September to December, and January to February 2013, the WLIS location imported heat at a rate of ∼25 W m^{-2} of areal surface. It is interesting to note that the rate of wintertime heat import due to horizontal exchange is less than half that of the summertime export, but lasts two times as long (September–February vs. May–July).

In addition to quantifying the horizontal heat exchange at the WLIS location, our results also offer insight into the spatial structure of the net surface heat fluxes and horizontal exchanges throughout LIS. Both the LIS-FVCOM hydrodynamic model and the SST observations that together form the basis of our results provide spatial coverage of the entire LIS region. Using bulk formulae to estimate heat fluxes, however, requires local meteorological data (Ilia et al., 2021). We did not consider benthic fluxes in our derived estimates. These fluxes are likely small, and are of order 10 W^{-2} in lakes with temperatures and depths similar to LIS (Fang & Stefan, 1996). We note,

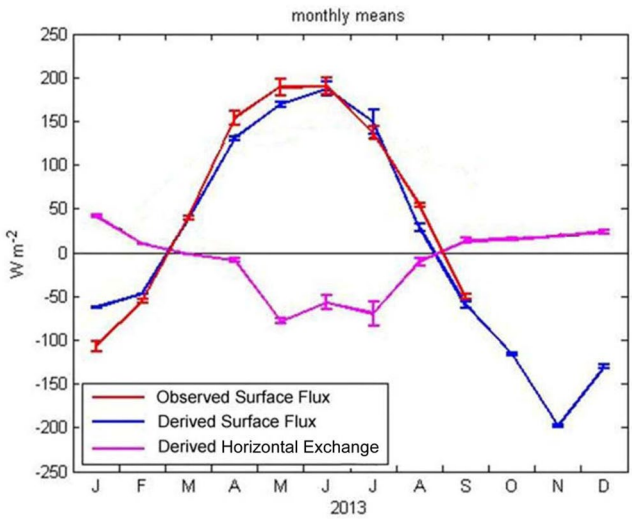

Figure 8. Comparison of Long Island Sound (LIS) 2013 surface heat flux estimates (W m^{-2}) at the location of the Western Sound buoy calculated from buoy observations (red) with those derived from the LIS FVCOM model using sea surface temperature (SST) assimilation (blue). Shown in magenta is the depth-integrated horizontal flux divergence (W m^{-2}). Error bars for the derived model estimates (blue and magenta) are based on the relative errors in the salt budget as discussed previously. Error bars for the bulk calculations from the buoy observations are ±5% (Fairall et al., 2003), McCardell and O'Donnell (2014) made data-based estimates of near-bottom along-channel horizontal exchanges of heat, oxygen, and salt from moored instruments at several locations in the western LIS. If integrated over a typical WLIS 10 m bottom layer depth, their results indicate a summertime (late July/early August 2004 and 2005) horizontal exchange in the WLIS region of -50 ± 60 W m^{-2} (per m^{-2} surface, see above), which is consistent with the summertime exchanges shown in the figure. Note, however, that McCardell and O'Donnell (2014) estimated the uncertainty as ±100% whereas the model-data synthesis results shown in the figure are an order of magnitude better. This figure also indicates that the derived surface fluxes may be slightly underestimated. This is consistent both with the small discrepancies that could arise out of not modeling benthic heat fluxes and with the methodology results shown in Figure 7 where we note a bias error of -8 W m^{-2} when recapturing prescribed fluxes.

however, that our results actually represent the sum of the surface and bottom boundary fluxes and that benthic fluxes into the water column would be expected to reduce the amplitude of the seasonal temperature cycle slightly and be of opposite sign to the surface fluxes. The magnitudes of our surface heat flux results may therefore be slightly underestimated.

Figure 9 shows our estimates of the spatial distribution of seasonal-mean depth-averaged temperatures and depth-integrated heat tendencies in LIS. Figure 10 shows plots of the spatial distribution of our estimates of the surface heat fluxes and horizontal exchanges plotted as the differences between these results and the seasonal means of these results (shown by the text in each plot). The results shown in both Figures 9 and 10 were spatially filtered using an 8 km Gaussian filter as described above.

During the winter and the summer, when horizontal exchange makes a significant contribution to the LIS heat budget, the flux divergence shows a strong spatial structure with the largest exchanges in both seasons occurring in the eastern portion of LIS. Figure 10 indicates that horizontal heat exchanges in the eastern LIS during winter and summer also impact the surface fluxes. In the winter, as warmer shelf water is brought into the Sound, surface heat losses due to latent, sensible, and long-wave radiation will increase in regions of warmer water due to an increase in the temperature differences between the air and the water. Likewise, during the summer, as cooler water is advected into LIS from the shelf, increased surface heat gains will occur in regions of cooler water. This is consistent with the observations of along and across Sound temperature gradients described in O'Donnell et al. (2014) and our results indicate that heat exchange in the eastern LIS creates strong spatial gradients in the surface heat fluxes during summer and winter. In 2013, summertime differences between our mean surface heat flux estimates in the eastern and western LIS regions are of order 100 W m^{-2} (Figure 10).

A primary limitation of our methodology is that the spatial scale of the SST assimilation data is considerably coarser than the model scale. Lombardo et al. (2016) discuss similar issues of spatial resolution mismatch in the context of using 32 km resolution North American Regional Reanalysis (NARR) SST output to initialize a 1-km resolution WRF model used to simulate coastal sea breezes in the LIS region. Our FVCOM-LIS model has a spatial resolution in LIS on the order of a few hundred meters to a kilometer, whereas the SST data we used for the temperature assimilation has a spatial resolution of 4 km. Because of the scale mismatch, fluxes in model regions with fine-scale spatial gradients can be misestimated when combined with coarser scale products. The summer panels of Figure 10 show an example of this problem in the vicinity of the Connecticut River plume (41.2 N, 72.4 E), where large horizontal advective fluxes due to baroclinic exchange are a primary driver of the estimates of the net surface fluxes. The lower resolution of the SST data (along with poor near-shore coverage) is also problematic for estimating local surface fluxes in near-shore regions. Low-pass filtering the results below the spatial scale of the SST data solves some of these problems, but also indicates that our results should not be used at finer scales in regions of steep gradients. Without further refinement, our methodology could not, for example, be used to examine the relative importance of autumnal cooling in near-shore shoals since near-shore water temperatures are simply not represented in the SST data.

6. Conclusions

Our LIS results indicate that it is possible to utilize remote-sensing SST data to make estimates of surface heat fluxes as the difference between the depth-integrated tendencies and the depth-integrated exchanges in a calibrated hydrodynamic model. Fairall et al. (2003) state that the original 1992 COARE goal was to develop flux algorithms that could yield monthly mean results within ±10 W m^{-2} of direct covariance measurements. This

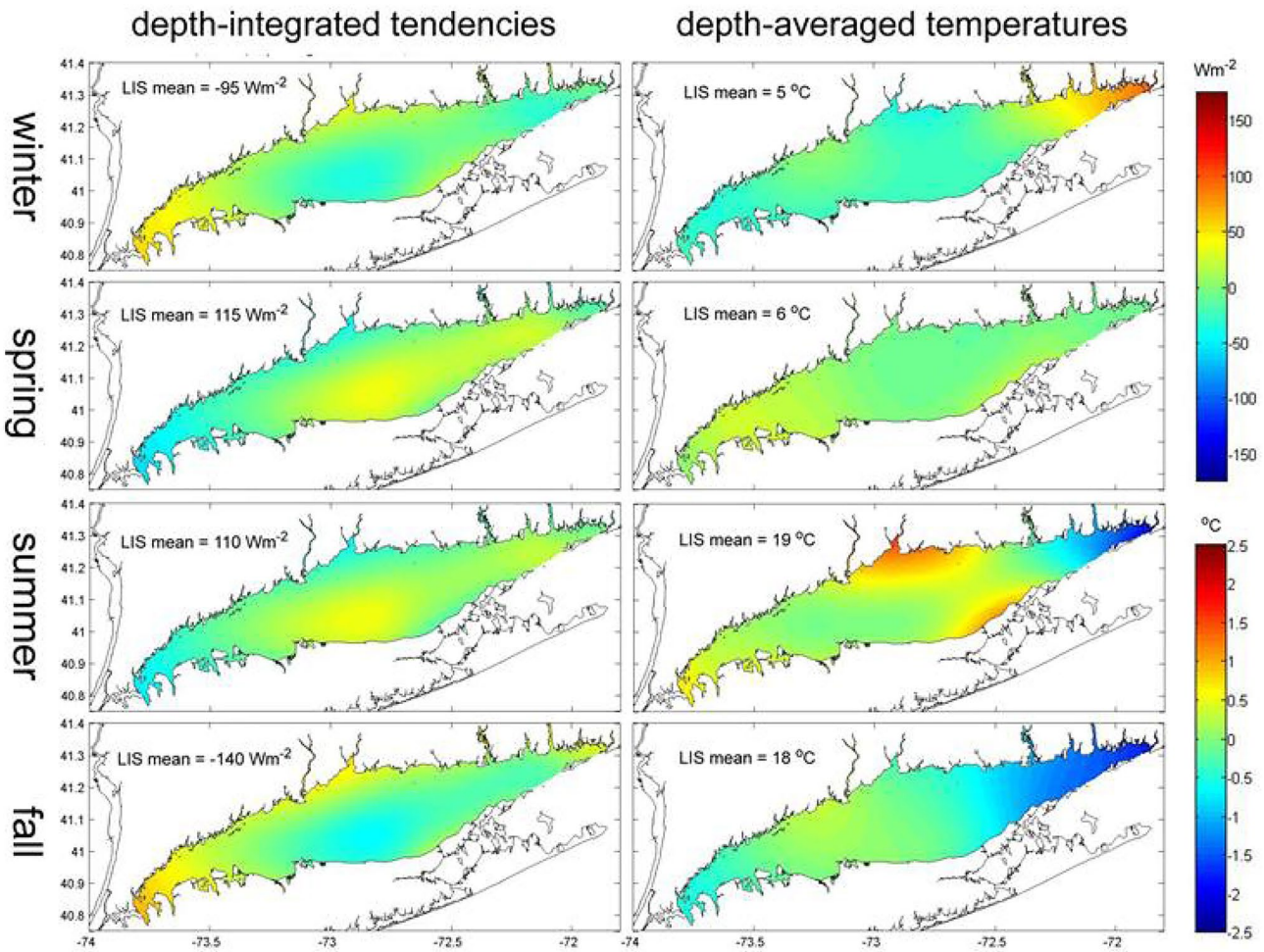

Figure 9. Spatial distributions of depth-integrated Long Island Sound (LIS) heat tendencies (left-hand plots, W m^{-2}) and depth-averaged temperatures (right-hand plots, °C) from the sea surface temperature assimilation model results. Winter, spring, summer, and fall are defined as December, January, and February; March, April, and May; June, July, and August; and September, October, and November, respectively. The results in each panel are shown as the deviation from the areal-averaged LIS mean shown by the text in each panel.

error is similar to our estimate of ±10 W m^{-2} RMS and −8 W m^{-2} bias errors in our methodology. As shown in Figure 7, the agreement of our derived surface fluxes with those estimated using COARE formulae is excellent, although we note that our methodology appears to slightly underestimate the late spring/early summer fluxes. These discrepancies could be a result of non-zero seasonal benthic fluxes and/or the tendency of the methodology to slightly underestimate large fluxes as seen in Figure 7. Although we have not done so, Figure 7 indicates that some systematic bias error could be corrected to further refine the methodology.

Unlike COARE estimates (or direct covariance measurements), our SST and model-derived results are not limited to a particular observational location and are therefore able to reveal spatial variability without the expense of an observational array. The methodology could also be useful in determining locations where further meteorological measurements would be valuable. As shown in Figure 10, our results indicate significant spatial structure of the surface heat fluxes in LIS. However, we were only able to compare our results with those from the WLIS buoy location (see Figure 1). To further validate or refine our methodology, it would therefore be worthwhile to make bulk estimates from measurements in the central and eastern LIS as well. The methodology is also limited by the spatial scale of SST observations. The 4 km resolution of the satellite SST is, however, considerably finer than the 32 km resolution of the NCEP NARR and the methodology described herein could be a valuable complement to NARR heat flux estimates.

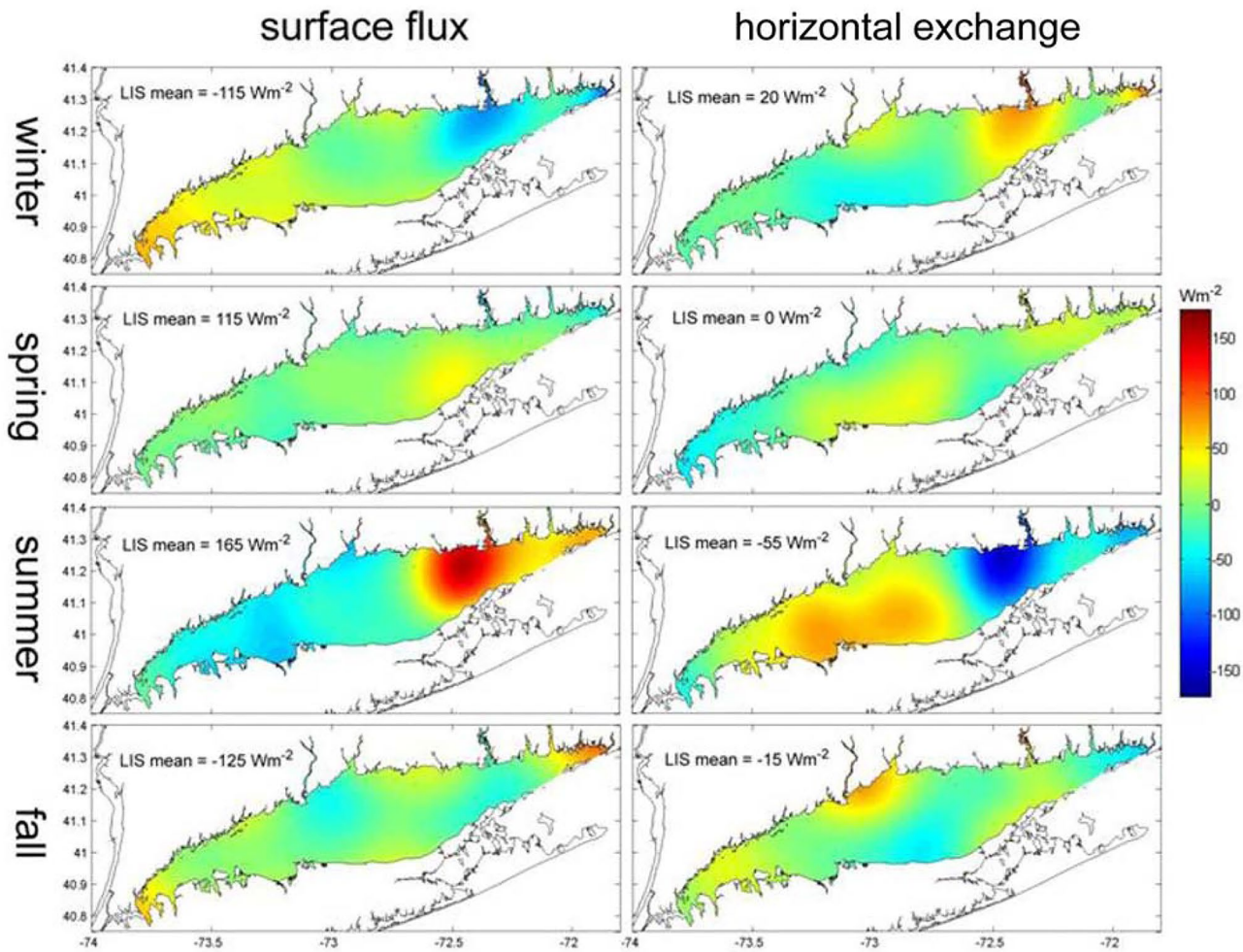

Figure 10. Spatial distributions of surface fluxes (W m^{-2}) and depth-integrated horizontal exchanges (W m^{-2}) from the sea surface temperature assimilation model results. Winter, spring, summer, and fall are defined as December, January, and February; March, April, and May; June, July, and August; and September, October, and November, respectively. The results in each panel are shown as the deviation from the areal-averaged Long Island Sound (LIS) mean shown by the text in each panel.

Data Availability Statement

The sea surface temperature data used in this paper can be obtained from NASA (https://podaac.jpl.nasa.gov/dataset/MODIS_AQUA_L3_SST_MID-IR_DAILY_4KM_NIGHTTIME_V2019.0) and the LISICOS ERDDAP server (http://merlin.dms.uconn.edu:8080/erddap/). The advice and help of Professor C. Chen of the University of Massachusetts, Dartmouth, were crucial to this project.

Acknowledgments
This work was supported by The Long Island Sound Study, a component of the National Estuary Program of the Environmental Protection Agency; NERACOOS, a Regional Information Coordination Entity of the National Oceanic and Atmospheric Administration's U.S. Integrated Ocean Observing System (Grant NA21NOS0120095); Connecticut Sea Grant, University of Connecticut (Project R/EM-3); the National Science Foundation (Grant 1756789); the Connecticut Department of Energy and Environmental Protection's Long Island Sound Habitat Mapping Initiative; and by the University of Connecticut.

References

Burchard, H., Bolding, K., & Ruiz-Villarreal, M. (1999). *GOTM, a general ocean turbulence model. Theory, implementation and test cases*. Report EUR 18745. European Commission.

Chen, C. H., Beardsley, R. C., Cowles, G., Qi, J., Lai, Z., Gao, G., et al. (2013). *An unstructured grid, finite-volume community ocean model: FVCOM user manual*. Marine Ecosystem Dynamics Modeling Laboratory.

Chen, C. H., Huang, H., Beardsley, R. C., Liu, H., Xu, Q., & Cowles, G. (2007). A finite-volume numerical approach for coastal ocean circulation studies: Comparisons with finite difference models. *Journal of Geophysical Research*, *112*(C3), C03018. https://doi.org/10.1029/2006JC003485

Codiga, D. L., & Ullman, D. S. (2011). Characterizing the physical oceanography of coastal waters off Rhode Island, Part 1: Literature review, available observations, and a representative model simulation. *Rhode Island Ocean Special Area Management Plan*, (Vol. 2). Chap. 2.

Egbert, G. D., Bennett, A. F., & Foreman, M. G. G. (1994). TOPEX/POSEIDON tides estimated using a global inverse model. *Journal of Geophysical Research*, *99*(C12), 24821–24852. https://doi.org/10.1029/94jc01894

Fairall, C. W., Hare, J. E., Grachev, A. A., & Edson, J. B. (2003). Bulk parameterization of air–sea fluxes: Updates and verification for the COARE algorithm. *Journal of Climate*, *16*(4), 571–591. https://doi.org/10.1175/1520-0442(2003)016<0571:bpoasf>2.0.co;2

Fang, X., & Stefan, H. G. (1996). Dynamics of heat exchange between sediment and water in a lake. *Water Resources Research*, *32*(6), 1719–1727. https://doi.org/10.1029/96wr00274

Ganju, N. K., Brush, M. J., Rashleigh, B., Aretxabaleta, A. L., del Barrio, P., GrearHarris, J. S., et al. (2016). Progress and challenges in coupled hydrodynamic-ecological estuarine modeling. *Estuaries and Coasts*, *39*(2), 311–332. https://doi.org/10.1007/s12237-015-0011-y

Gay, P., O'Donnell J, J., & Edwards, C. A. (2004). Exchange between Long Island Sound and adjacent waters. *Journal of Geophysical Research*, *109*(C6), C06017. https://doi.org/10.1029/2004JC002319

Georgas, N., Yin, L., Jiang, Y., Wang, Y., Howel, P., Saba, V., et al. (2016). An open-access, multi-decadal, three-dimensional, hydrodynamic hindcast dataset for the Long Island Sound and New York/New Jersey Harbor Estuaries. *Journal of Marine Science and Engineering*, *4*(3), 48. https://doi.org/10.3390/jmse4030048

Ilia, A., McCardell, G., Howard-Strobel, K., & O'Donnell, J. (2023). Observations of autumnal cooling in a large estuary. *Journal of Geophysical Research: Oceans*, *128*, e2022JC018586. https://doi.org/10.1029/2022JC018586

Jia, Y., & Whitney, M. M. (2019). Summertime Connecticut river water pathways and wind impacts. *Journal of Geophysical Research*, *124*(3), 1897–1914. https://doi.org/10.1029/2018JC014486

Kaputa, N. P., & Olsen, C. B. (2000). Long Island Sound ambient water quality monitoring program: Summer hypoxia monitoring survey '91–'98 data review. Report. Connecticut Department of Energy and Environmental Protection.

Lee, Y. J., & Lwiza, K. (2005). Interannual variability of temperature and salinity in shallow water: Long Island Sound, New York. *Journal of Geophysical Research*, *110*(C9), C09022. https://doi.org/10.1029/2004JC002507

Lombardo, K., Sinsky, E., Jia, Y., Whitney, M. M., & Edson, J. (2016). Sensitivity of simulated sea breezes to initial conditions in complex coastal regions. *Monthly Weather Review*, *144*(4), 1299–1320. https://doi.org/10.1175/MWR-D-15-0306.1

McCardell, G., & O'Donnell, J. (2014). Estimates of horizontal fluxes of oxygen, heat, and salt in Western Long Island Sound. *Journal of Geophysical Research: Oceans*, *119*(10), 7267–7276. https://doi.org/10.1002/2014JC009904

OBPG (2015). *MODIS Aqua global level 3 mapped SST. Ver. 2014*.0. PO.DAAC. https://doi.org/10.5067/MODAM-8D9N4

O'Donnell, J. (2015a). *Physical oceanography of Eastern Long Island Sound region: Field report (draft)*. Prepared by the University of Connecticut, with the support from Louis Berger. Prepared for the Connecticut Department of Transportation. (August 2014).

O'Donnell, J. (2015b). *Physical oceanography of Eastern Long Island Sound region: Modeling report (draft)*. Prepared by the University of Connecticut, with the support from Louis Berger. Prepared for the Connecticut Department of Transportation. (August 2014).

O'Donnell, J., Wilson, R. E., Lwiza, K., Whitney, M., Bohlen, W. F., Codiga, D., et al. (2014). The physical oceanography of Long Island Sound. In J. S. Latimer, M. A. Tedesco, R. L. Swanson, C. Yarish, P. E. Stacey, & C. Garza (Eds.), *Long Island Sound: Prospects for an Urban Sea*. Springer.

Pawlowicz, R., Beardsley, B., & Lentz, S. (2002). Classical tidal harmonic analysis including error estimates in MATLAB using T_TIDE. *Computers & Geosciences*, *28*(8), 929–937. https://doi.org/10.1016/s0098-3004(02)00013-4

von Storch, H., & Zwiers, F. W. (1999). *Statistical analysis in climate Research*. Cambridge University Press.

Wilson, R. E., Crowley, H. A., Brownawell, B. J., & Swanson, R. L. (2005). Simulation of transient pesticide concentrations in Long Island Sound for late summer 1999 with a high resolution coastal circulation model. *Journal of Shellfish Research*, *24*, 865–875.